On the use of ultrasound for fluid-structure interaction studies of the ascending aorta

Sonja Pejcic[1][*]**, Mohammad Reza Najjari**[1]**, Kai Zhang**[1]**, Gianluigi Bisleri**[2]**, David E. Rival**[1]

[1] Queen's University, Department of Materials and Mechanical Engineering, Kingston, Canada

[2] Kingston General Hospital, Division of Cardiac Surgery, Kingston, Canada

[*] sonja.pejcic@queensu.ca

Abstract

The feasibility of ultrasound to characterize elasticity is explored through dynamic testing of a non-linear elastic reference material under cylindrical loading conditions. The vessel was subjected to three cosine flow profiles, at peak Reynolds numbers (Re) of 1500, 2000, and 2500, in addition to three steady cases at the same Reynolds numbers. Ultrasound images are used to calculate the velocity field through the compliant test section, and the change in diameter of the vessel over time. Pressure is extracted from the ultrasound imaging velocimetry results, and is used to find the pressure-area relationship. The extracted pressure matched with the pressure sensor data located upstream of the compliant section, with some fluctuations. Two constitutive laws, the Laplace law and the relation by Olufsen (1999), were implemented to find instantaneous elastic modulus, E. The results are compared to a tensile test of the elastic material, where the elastic modulus steadily decreased over the strain range. The Laplace law over-predicts the elasticity, and indicated a significant increase in E at higher strains. The relation by Olufsen (1999) also over-predicts the value of E, though to a lesser extent, and show good agreement in trend over the strains of interest. To consider a correction factor to Olufsen's relation, more data for different flow profiles and higher flow rates will need to be explored. The results demonstrate promise that ultrasound can be used as a stand-alone tool for *in vitro* and *in vivo* fluid-structure interactions studies of the ascending aorta.

1 Introduction

Biological tissues, though subject to conservation of mass, momentum, and energy, are governed by unique constitutive equations that differentiate them from inorganic materials, and thus make them harder to characterize. To fully understand the complexity of the vascular wall and the mechanisms that may lead to cardiovascular complications, the fluid-structure interactions (FSI) — for example, surface deformation of and wave propagation in arterial walls, local hemodynamics, and temporal wall shear stress — must be considered. Periods of disturbed blood flow can arise and may cause abnormal FSI within the ascending aorta, leading to progressive mechanical deterioration, which is linked to aneurysm initiation (Malek and Alper, 1999). In such conditions, recirculating flow is observed on the inner curve of the ascending aorta. Depending on the aortic valve geometry, a jet can impinge on the upper area of the ascending aorta. Mechanical bi-leaflet replacement valves can yield even more complex flow by generating three interacting jets (Miron et al., 2014).

Use of ultrasound to obtain particle image velocimetry data within opaque structures has been rapidly increasing in recent years (referred to as ultrasound imaging velocimetry, UIV), though its resolution, particularly within the near-wall region, remains inferior to that of optical techniques (Poelma, 2017). Ultrasound images obtained for UIV analysis also hold data pertaining to wall thickness, diameter, and surface deformation along a single plane. To date the use of ultrasound for FSI studies has not been explored. The dynamic nature of the vasculature poses a challenge to typical surface reconstruction techniques. Compared to numerical analyses, few experimental investigations on pulsatile flows in elastic vessels are known.

The primary goal of this study is to characterize mechanical properties from a dynamic cylindrical loading scenario in an *in vitro* setting. This will also contribute to understanding the pressure-area ($p-A$)
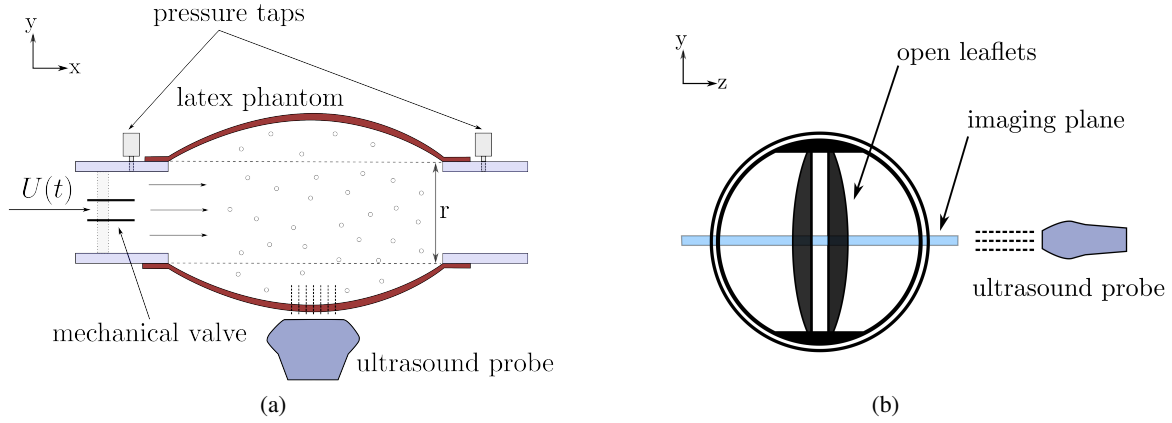
Figure 1: (a) Close-up of the compliant section within the flow loop. Pressure sensors are installed right before the compliant tube attachments, with the valve located 50 mm upstream from the start of the compliant tube. The y- and x- lengths are normalized by r, where $y = 0$ at the centerline. The flow is seeded with micro-bubbles which reflect the ultrasound waves. (b) The probe is oriented with respect to the valve such that the imaging plane is perpendicular to the open leaflets.

relationship for elastic materials. Another goal of the current study is to explore the use of ultrasound for general FSI studies, and to eventually implement ultrasound as a stand-alone tool to characterize the ascending aorta *in vivo*. With knowledge of the loading resulting from fluid forcing (i.e., estimated through pressure) and wall movement in response to different flow patterns, we can further our understanding of biological FSI, and extract material properties to better inform clinical practice.

2 Methodology

Experimental Setup

Experiments were performed using a custom flow loop incorporating an opaque latex phantom for the test section submerged within an optical tank. Figure 1(a) shows a close-up of the compliant section. For this initial study, curvature of the vessel has been neglected. A fully programmable pump (MCP-Z Process, Ismatec) is used to generate flow, where the working fluid is water. The pressure upstream and downstream of the compliant section was measured at 1000 Hz using two Omega PX409 sensors.

Six pulsatile test cases with a cosine waveform were performed in addition to three steady cases at the same Reynolds numbers. The non-dimensional parameters chosen for this experiment are: (1) $Re = 1500$, $St = 0.19$, (2) $Re = 2000$, $St = 0.14$, and (3) $Re = 2500$, $St = 0.09$, where the Strouhal number is defined as $St_{peak} = f U_{peak}/D$, with D as the initial diameter of the compliant tube. The frequency chosen for the pulsatile cases corresponds to an *in vivo* heart rate of 75 beats per minute, representing a resting state. For future clinically targeted studies, the latex test section will be replaced with a piece of the ascending aorta. A mechanical bi-leaflet valve identical to the one analyzed in Miron et al. (2014) was used at the entrance condition to replicate conditions within a simplified cardiovascular circuit. The orientation of the valve with respect to the imaging plane has a significant effect on the flow observed (Gülan and Holzner, 2018). Figure 1(b) shows the probe oriented such that the field of view (FOV) was perpendicular to the valve leaflets when open.

Ultrasound Particle Image Velocimetry

In order to perform ultrasound particle image velocimetry (UIV), the flow was seeded with Definity contrast agent (perflutren injectable suspension). Particle image density was carefully adjusted to obtain high quality images. B-mode ultrasound images are acquired using SonixTouch Q+ (Research) with L14-5/38 linear ultrasound probe. Ultrasound settings (i.e., dynamic range, gain, power, frequency) were adjusted to have high contrast images. The rejection setting in ultrasound imaging was set to zero and gain was adjusted to

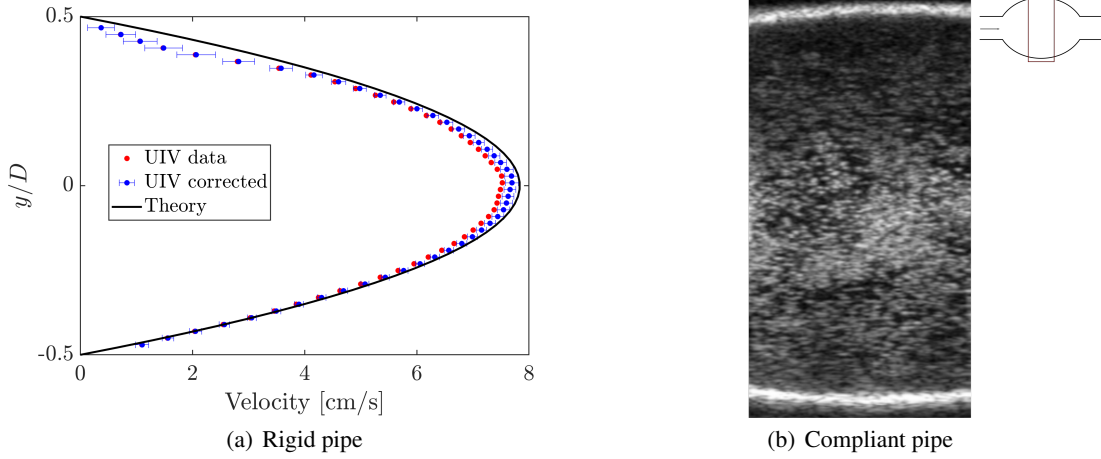(a) Rigid pipe

(b) Compliant pipe

Figure 2: (a) Velocity profile for a steady flow within a rigid pipe as part of a different flow loop. A correction to account for the beam sweep velocity (outlined in Poelma, 2017) was applied to this set of data. (b) Raw image showing flow within the compliant test section (steady, $Re = 2500$), where the width of the FOV is 19.2 mm and it is centered away from the rigid boundaries.

be around 20%. To achieve a high frame rate only 50% of the sector were used, resulting in 125 frames per second with a line density of 192 and depth of 4.2 cm. This enabled measurement of flow rates with a maximum of 20 pixel particle displacements. To validate the UIV system, a fully developed laminar flow in a rigid pipe was tested and results are compared with Poisuelle velocity profile shown in Figure 2(a). This showed a good match (within 5%) between experimental and theoretical velocities. The field of view (FOV) for the compliant pipe is shown in Figure 2(b).

Due to wall motion in pulsatile flows, a MatLab script was first used to detect the elastic wall in each frame, and automatically masked the images to enhance the background subtraction during the image processing step. Acquired images were then processed using Davis 8.4 (LaVision) to obtain velocity maps. Background noise was reduced by subtracting a Gaussian sliding average filter; then, the PIV sliding sum-of-correlation algorithm with a time filter length of three frames was used to achieve velocity results with high certainty. A multi-pass option with decreasing window size, from 64 to 24 pixels with 75% overlap in the last step was used. Since the primary reason for obtaining velocities was to extract pressure which requires velocity gradients, we used 75% overlap in the last step to increase spatial resolution of the second-order central difference derivatives. In the vector post-processing step, allowable displacement range, correlation peak ratio, and median filters were applied. Velocity results were also smoothed using a 3x3 smoothing function.

Pressure Extraction

The pressure field was extracted from the UIV results with integration of the Navier-Stokes equations where body force and viscous terms ($Re \gg 1$) are neglected:

$$\nabla p = -\rho \frac{D\mathbf{u}}{Dt} \tag{1}$$

where ρ is the density of the working fluid, and $D\mathbf{u}/Dt$ is the material derivative. The result from spatial integration is highly dependent on the pathway (Van Oudheusden, 2013). As such, for all test cases the pressure along the centre line was first established using $\partial p/\partial x$, with the reference pressure obtained from the upstream sensor. The pressure in the y-direction along each column was then found through integration of $\partial p/\partial y$ starting from the centre line. The area of interest (AOI) for the steady cases is taken as two columns and two rows smaller than the FOV of the ultrasound, while the optimal AOI for the pulsatile cases is found for each frame based on the velocity map.

Elasticity Characterization

The typical value of elastic modulus for latex at a thickness of 0.5 mm is 1 ± 0.25 MPa reported at 500% strain. Since the strains of interest are significantly lower (up to 45%), a uniaxial tensile test of a dog-bone sample of the latex was performed with a BOSE Instron machine. Many studies concerning the mechanical properties of the ascending aorta involve the use of static inflation tests and report the resulting pressure-diameter relationship to deduce elastic properties (Avanzini et al., 2014). The three steady cases collected in this study are analyzed in the same manner as the pulsatile ones for direct comparison between characterization under dynamic and static conditions. In order to describe the deformation in elastic tubes, the internal pressure and cross-sectional area are needed. Note that latex is not a linearly elastic material. To describe classical non-linear elasticity, an instantaneous elastic modulus is taken based on the Laplace law, which associates an infinitesimal change in the vessel radius to the change in transmural pressure (Fung, 1996):

$$E = \frac{\partial p}{\partial R} \frac{R^2}{h} \tag{2}$$

where p is the transmural pressure, obtained from the upstream pressure sensor readings, R is the instantaneous radius calculated from the ultrasound images, and h is the thickness of the wall. There is a trade-off between accuracy in edge detection and image quality for UIV, as ideal ultrasound settings for particle detection (i.e. gain, rejection number) are not the ideal settings for wall thickness detection. Thus, the instantaneous wall thickness could not be resolved from the ultrasound images and so this value remained fixed over the entire strain range. For analysis, the partial derivative of pressure with respect to radius is treated as a difference, $\Delta p / \Delta r$, with reference to no flow conditions, in order to be able to compare the steady and pulsatile cases. The instantaneous radius, r, is calculated at the middle of the FOV (assumed to be the maximum radius at the furthest point from the rigid boundary conditions) through edge detection. Error of these values is reported to be ± 1 mm.

Typical non-linear $p - A$ relationships take the form of:

$$\Delta p = \beta (\sqrt{A} - \sqrt{A_o}) \tag{3}$$

where β is a coefficient provided by various constitutive relations incorporating elastic modulus, E. Given that area and pressure are experimentally recorded, β and the resulting E value can be solved for. The β parameter used for this study was introduced by Olufsen (1999):

$$\beta = \frac{4}{3} \frac{E h}{R_o} \frac{1}{\sqrt{A}} \tag{4}$$

As explained in Figure 3, the Laplace law only accounts for uniform expansion, which is an assumption made for this preliminary study.

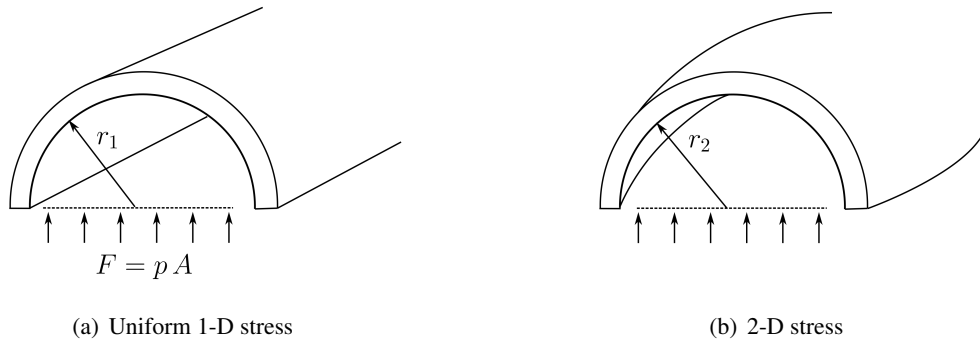(a) Uniform 1-D stress   (b) 2-D stress

Figure 3: (a) The Laplace law assumes a one-dimensional stress state for an infinite pipe undergoing an axi-symmetric, uniform expansion, where r_1 is assumed to solely describe the expansion along the length of the pipe, L. The force exerted on the walls of the pipe can be related to internal pressure by the area, $2r_1 L$. (b) For a finite pipe length with boundaries fixed to rigid sections and no absolute longitudinal movement, the expansion may be axi-symmetric, though it will not be uniform due to bulging. This results in a two-dimensional stress state, where r_2 varies with the length of the pipe.

3 Results and Discussion

Steady Flow

Figure 4 shows the velocity fields for the three steady cases of $Re = 1500$, 2000, and 2500. The total area of the elastic vessel increases by 17% and 59.6% for $Re = 2000$ and 2500, respectively, as compared to $Re = 1500$. Since the jet area remains relatively the same between the three cases, there is an increase in the size of the re-circulation zone arising from the expansion. The mechanical valve introduces three jets into the flow; however, since the ultrasound FOV is 50 mm downstream of the valve, the jets have already mixed together making them indiscernible while introducing turbulent fluctuations.

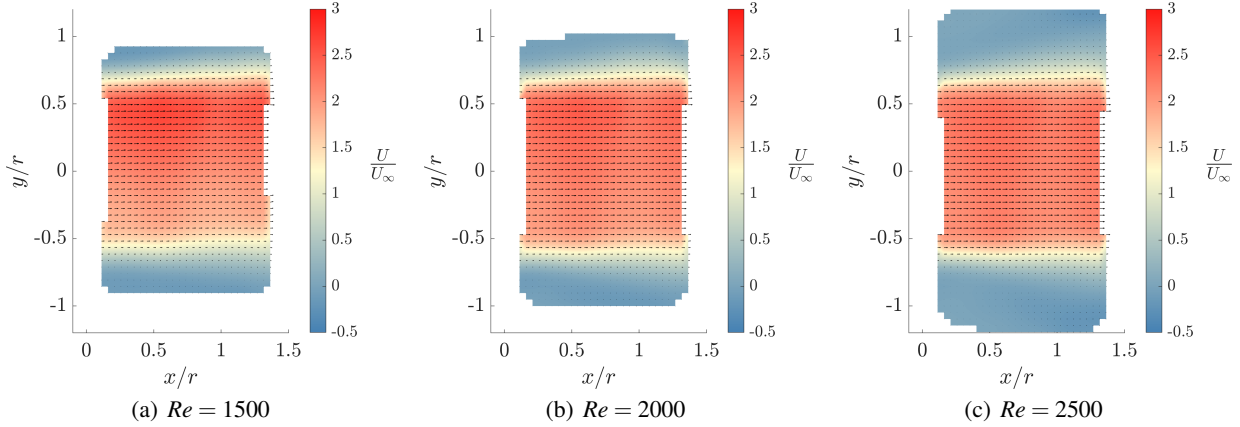(a) $Re = 1500$ (b) $Re = 2000$ (c) $Re = 2500$

Figure 4: Velocity profile, normalized by the peak velocity for each case, for a steady flow through the compliant section. While the vessel is expanding with increasing Re, the jet width stays relatively the same, yielding a larger re-circulation zone.

The pressure field for the steady cases is presented in Figure 5, and exhibits a similar trend between the three Re numbers, showing two distinct regions: an initial uniform decrease across the area of interest (AOI), followed by an equivalent increase. There is an overall decrease in pressure downstream (as measured from the difference between the left most and right most columns in the AOI).

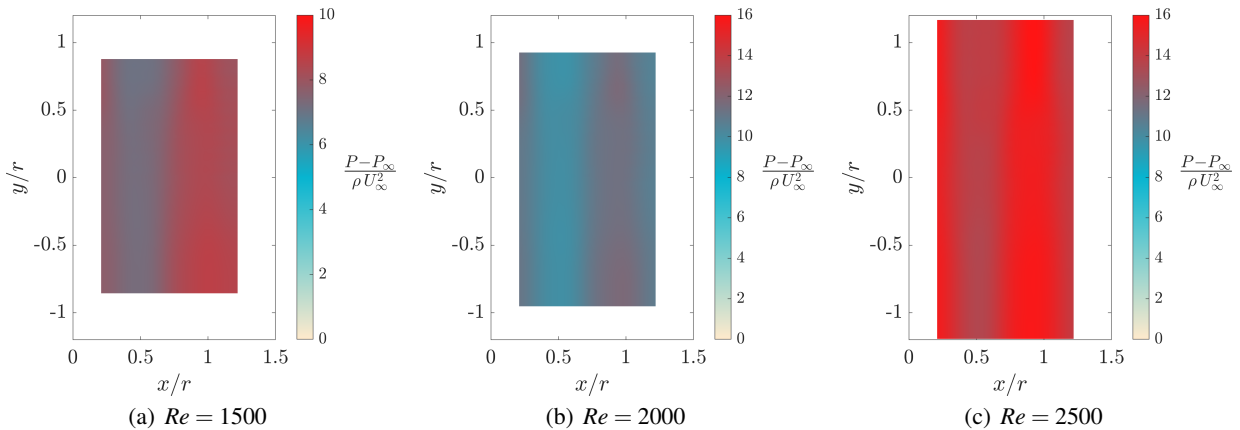(a) $Re = 1500$ (b) $Re = 2000$ (c) $Re = 2500$

Figure 5: Pressure field integrated vertically from the centre line, for an averaged steady flow through the compliant section. Note the difference in scale for (a) to showcase the trend across the field. There is an overall decrease in pressure across the FOV.

Table 1 compares the pressure drop extracted from UIV to the theoretical pressure drop for a rigid pipe calculated from the Hagen-Poiseulle equation. The pressure drop is expected to be higher in a compliant

tube than a rigid one, and we see this reflected in the experimental data.

Table 1: Pressure drops for steady cases, where the theoretical ΔP is calculated from the Hagen-Poiseulle equation for a rigid pipe with a length of 19.2 mm, which corresponds to the width of the FOV. Pressure extraction from UIV was performed over the entire length of the FOV.

Re	ΔP [Pa] Theoretical	ΔP [Pa] UIV
1500	0.045	1.35
2000	0.059	1.66
2500	0.074	2.52

Pulsatile Flow: Pressure and Velocity Field

The absolute pressure at the upstream location was used as the boundary condition for pressure extraction. The pressure data recorded from this sensor is in phase with the cyclic diameter expansion that is obtained from the ultrasound images. Figure 6 shows the pressure profile from the sensor as well as the extracted pressure over time, using phase-averaged UIV results across six cycles, and filtered using a Savitzky-Golay filter. Figure 7 shows instantaneous velocity and pressure fields for the three pulsatile flow cases at the same point of the pressure cycle as illustrated in Figure 6. Analysis of instantaneous velocities shows good repeatability in the jet formation between cycles and Re values. The lag between pressure and velocity increases as Re is increased. Although the velocities in Figure 7 are plotted at the same phase of the pressure signal, they do not correspond to same phase of the flow rate. As a result, $Re = 1500$ shows flow during acceleration, $Re = 2000$ shows the velocity after the peak flow rate, and the flow for $Re = 2500$ is during mid deceleration where velocity has already significantly decreased.
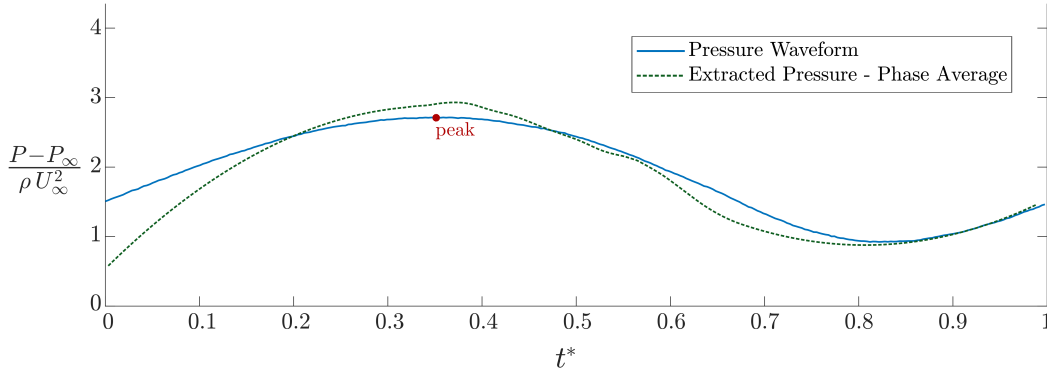

Figure 6: General pressure waveform recorded over one cycle for each test case, values shown for $Re = 2000$. The red dot highlights the peak of the cycle ($t^* = 0.35$) at which the snapshots in Figure 7 are taken. The pressure waveform is synchronized with the diameter expansion. Phase-averaged UIV results are used for the pressure calculation. The extracted pressure at each time step is averaged along the y-direction at $x/r = 0.75$ and a Savitzky-Golay filter is applied to the data.

During acceleration, higher frequency oscillations indicating drops in pressure are present throughout the extracted pressure, likely following structures passing through the FOV, and causing a significant under-predication of the pressure waveform between $0 < t^* < 0.2$. There is not a single frequency component associated with vortex shedding, due to the 3D flow caused by the valve and the increase of the re-circulation region throughout a cycle. In theory, an elastic cylinder should respond to these locally focused pressure perturbations, though it is probable that the finite test section alongside the rigid boundaries prevent the material from doing so.
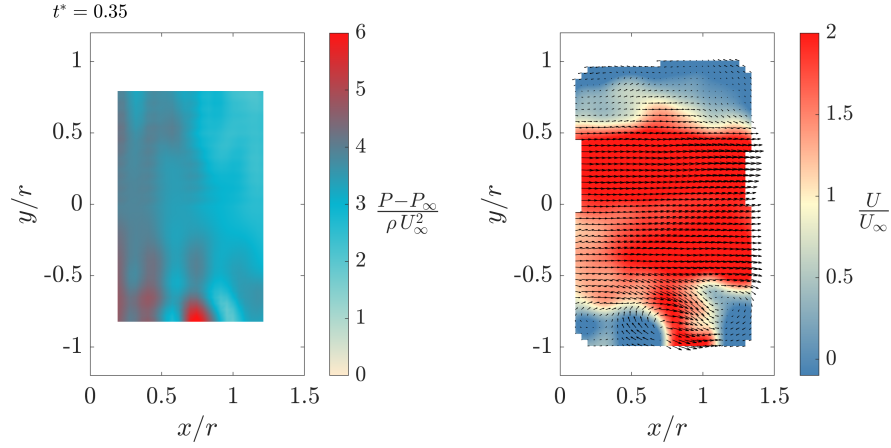
(a) *Re* = 1500
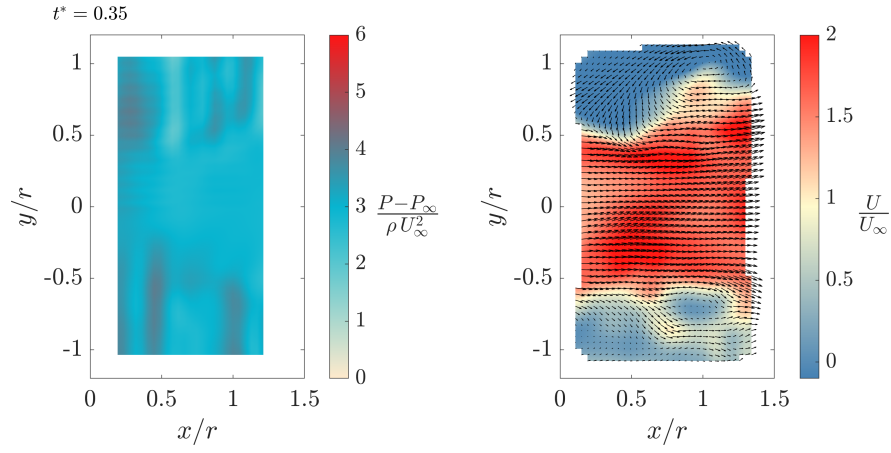
(b) *Re* = 2000
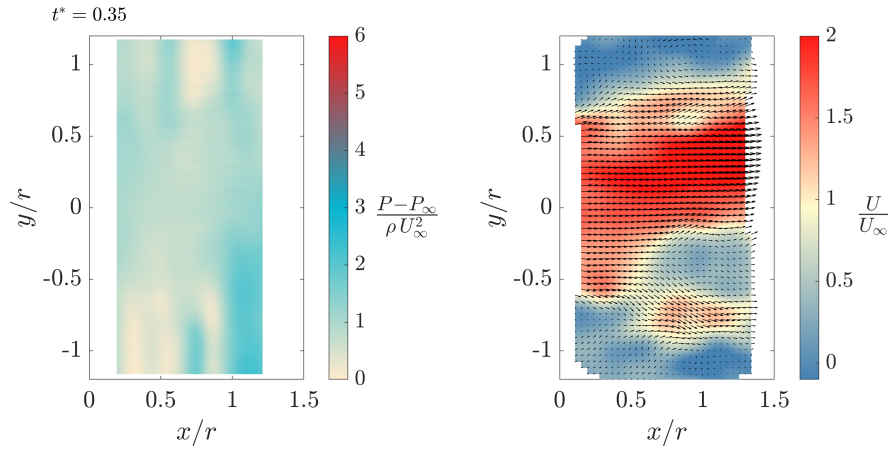
(c) *Re* = 2500

Figure 7: Extracted pressure field and instantaneous flow field at the peak of the pressure waveform, $t^* = 0.35$. The velocities are normalized using the theoretical peak flow velocity for each *Re* number. Pressure field is obtained by integrating Equation 1 vertically from the centre line.

In addition, the error associated with the accuracy and resolution of the ultrasound (i.e., the blurring of the edges) may have prevented detection of small oscillations between each time step. We can conclude that the force on the walls causing expansion is largely due to the pressure driving the flow rather than the

pressure arising from transient fluid structures. Figure 8 shows the transmural pressure versus strain for the loading portion of a cycle. These data was used to calculate elasticity.
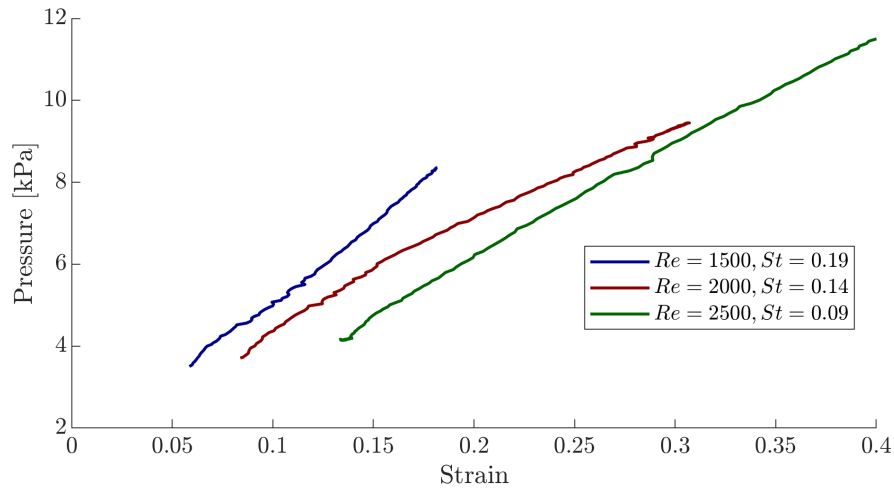

Figure 8: Transmural pressure versus strain for the three pulsatile cases. While it would be expected that the lines are parallel, each Re value has a slightly different slope, arising from error in the extracted pressure. The vertical offset between the lines can also be attributed to this.

Elasticity Calculations

Figure 9 shows the instantaneous elastic modulus, E, for the steady cases found from the two constitutive relations presented earlier. Using Laplace law from Equation 2, there is a very small increase in E, rising by 0.36% and 1.44% respectively between the three Re values. The constitutive relation by Olufsen (1999) in Equation 3 – 4 predicts a more elastic material than the Laplace law, with a decreasing E over the strain domain.
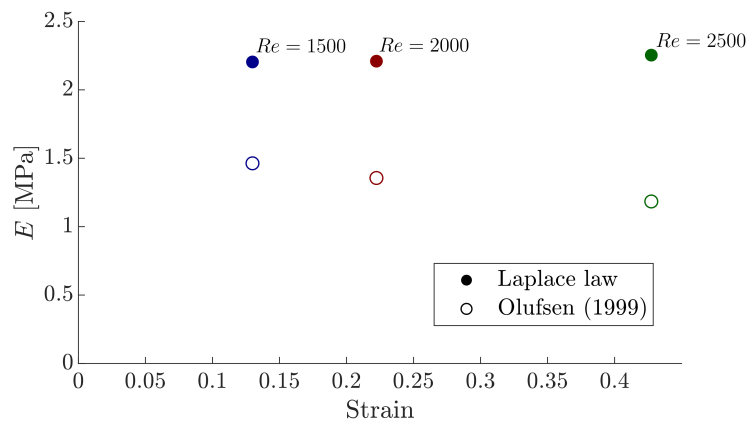

Figure 9: Instantaneous E versus strain for the three steady cases. Values represented by solid circles are calculated from the Laplace law, while hollow circles show the elasticity trend according to Olufsen (1999). The results from Laplace law show a very small increase across Re values, while Olufsen (1999) indicates a decrease in E.

Figure 10 shows the results for the pulsatile cases, where the constitutive relation by Olufsen (1999) also indicates a more elastic material than the Laplace law. Focusing on E calculated from the Laplace law for the pulsatile cases, we can observe a relatively steady value of E at $Re = 2000$, while for $Re = 1500$ the trend follows a parabolic trend with an initial decrease from 5% strain to 10% strain. $Re = 2500$ does not follow

either of these trends but rather shows a steady linear increase in E with strain. The initial steep decrease in E seen in the $Re = 1500$ case is present in both constitutive laws used, which may have resulted from error within the pressure-diameter relationship.
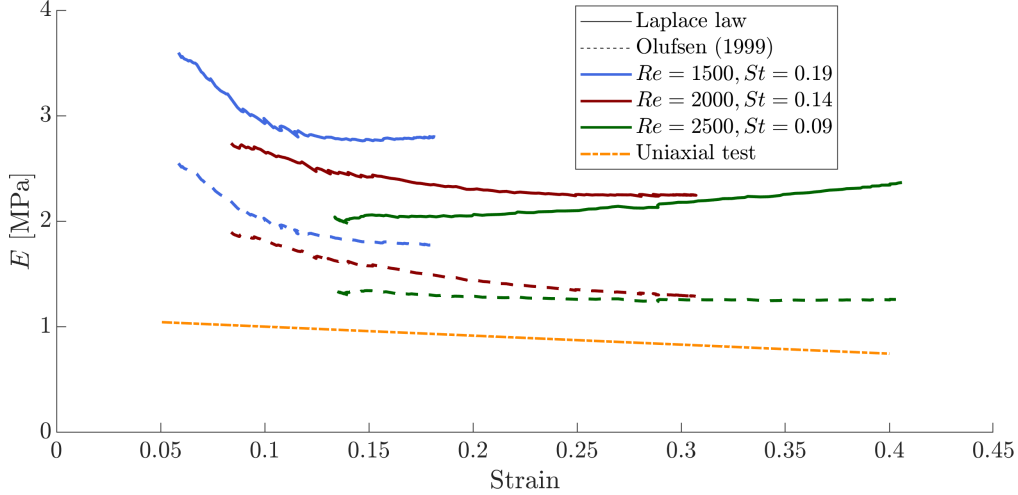

Figure 10: Instantaneous elastic modulus from a uniaxial tensile test of the latex material in comparison to instantaneous elastic modulus calculated over each pulsatile case. Solid lines represent E calculated from Laplace law, and dotted lines are the elastic modulus found from Olufsen's β parameter. Particularly throughout the strains over $Re = 2000$, Olufsen (1999) follows the slope of the uniaxial testing result, though higher by around 0.4 MPa.

While Olufsen (1999) over-predicts the elastic modulus in comparison to the values calculated from a uniaxial test on the same material over the same strains, the trends agree between the two loading conditions for $Re = 1500$ and 2500, showing a decrease in E as also observed over the steady cases. However, at a Reynolds number of 2500 there is a slight increase with higher strain. This trend likely stems from error within the pressure extraction, as particle displacements were quite high at this Reynolds number and the frame-rate of the ultrasound remained fixed throughout the test cases.

The experimental setup does not allow for a uniform cylindrical expansion. The length of the compliant section, and the resulting proximity of the area of interest (refer to Figure 2(b)) to the rigid boundaries, introduces 2D stresses (see Figure 3) which are not accounted for in the calculation of elastic modulus per the relations introduced in Equation $2 - 4$. Without consideration of these extra stresses when converting the internal pressure to stress through the derivation of the Laplace law, a higher value of E would be predicted, indicating a stiffer material.

4   Conclusions

A non-linear elastic opaque material was analyzed under cylindrical loading conditions where it was subjected to steady and pulsatile flows. Ultrasound imaging was used to capture compliant vessel deformation and obtain instantaneous planar velocities from UIV. Pressure sensors upstream and downstream of the flow were used to record the pressure over a cycle. The pressure waveform was synchronized with the diameter expansion. From the UIV results, the planar pressure field was extracted through integration of the Navier-Stokes equations, using the upstream sensor readings as the boundary conditions. The raw extracted pressure is seen to highlight structures as they pass through the FOV while following the greater trend from the pressure driving the flow; after phase averaging UIV results and applying a Savitzky-Golay filter on the resulting pressure field, the extracted pressure was used to calculate the $p - A$ relation.

Elasticity was calculated using two $p - A$ relationships: Laplace law (Fung, 1996), and that presented in Olufsen (1999). The trend of instantaneous elastic modulus between the values obtained from Olufsen's $p - A$ relation from dynamic testing and E calculated from uniaxial testing of the latex material indicates good agreement, though the magnitude of E is over-predicted. Both steady and pulsatile flow cases show relatively the same magnitudes of E at the same strain for both relations. While general comparisons are

drawn between the cylindrical and tensile configurations, it should not be expected that the material would have the exact same values of elastic modulus under these distinct loading conditions. It is expected there will be a significant difference in the loading and unloading pressure-diameter relationship when working with the ascending aorta, which exhibits viscoelasticity. This will need to be accounted for during the reporting of elastic modulus. After filtering, the extracted pressure was in good agreement with the experimentally measured pressure waveform and it was possible to calculate elasticity with relative accuracy. With further refinement on the extraction method used, ultrasound can be developed into a stand-alone device for FSI experiments. Of the two relations presented in this study, Olufsen's captures the behavior over the entire strain domain better than the Laplace law, particularly that at strain levels between 10% and 30%. A correction factor to account for lower strains and the difference in magnitude will be explored moving forward, in addition to comparison between other $p - A$ relationships. The results for this non-linear elastic material are promising for analysis of the ascending aorta, both *in vitro* and *in vivo*.

Acknowledgements

References

Avanzini A, Battini D, Bagozzi L, and Bisleri G (2014) Biomechanical evaluation of ascending aortic aneurysms. *Biomed Res Int*

Fung YC (1996) *Biomechanics: Circulation*. Springer-Verlag Berlin. 2nd ed. edition

Gülan U and Holzner M (2018) The influence of bileaflet prosthetic aortic valve orientation on the blood flow patterns in the ascending aorta. *Medical Engineering and Physics* 60:61–69

Malek AM and Alper SL (1999) Hemodynamic Shear Stress and Its Role in Atherosclerosis. *The Journal of the American Medical Association* 282:2035–2042

Miron P, Vétel J, and Garon A (2014) On the use of the finite-time Lyapunov exponent to reveal complex flow physics in the wake of a mechanical valve. *Experiments in Fluids* 55:1–15

Olufsen MS (1999) Structured tree outflow condition for blood flow in larger systemic arteries. *American Journal of Physiology-Heart and Circulatory Physiology* 276:H257–H268

Poelma C (2017) Ultrasound Imaging Velocimetry: a review. *Experiments in Fluids* 58:1–28

Van Oudheusden BW (2013) PIV-based pressure measurement. *Measurement Science and Technology* 24